nature materials

SUPPLEMENTARY INFORMATION
https://doi.org/10.1038/s41563-019-0369-5

In the format provided by the authors and unedited.

Anisotropic spin fluctuations in detwinned FeSe

Tong Chen[1], Youzhe Chen[2], Andreas Kreisel[3], Xingye Lu[4*], Astrid Schneidewind[5], Yiming Qiu[6], J. T. Park[7], Toby G. Perring[8], J Ross Stewart[8], Huibo Cao[9], Rui Zhang[1], Yu Li[1], Yan Rong[4], Yuan Wei[10], Brian M. Andersen[11], P. J. Hirschfeld[12], Collin Broholm[2,6] and Pengcheng Dai[1,4*]

[1]Department of Physics and Astronomy, Rice University, Houston, TX, USA. [2]Department of Physics and Astronomy, Johns Hopkins University, Baltimore, MD, USA. [3]Institut für Theoretische Physik, Universität Leipzig, Leipzig, Germany. [4]Center for Advanced Quantum Studies and Department of Physics, Beijing Normal University, Beijing, China. [5]Forschungszentrum Jülich GmbH, Jülich Center for Neutron Sciences at MLZ, Garching, Germany. [6]NIST Center for Neutron Research, National Institute of Standards and Technology, Gaithersburg, MD, USA. [7]Heinz Maier-Leibnitz Zentrum (MLZ), Technische Universität München, Garching, Germany. [8]ISIS Facility, STFC Rutherford-Appleton Laboratory, Didcot, UK. [9]Neutron Scattering Division, Oak Ridge National Laboratory, Oak Ridge, TN, USA. [10]Institute of Physics, Chinese Academy of Sciences, Beijing, China. [11]Niels Bohr Institute, University of Copenhagen, Copenhagen, Denmark. [12]Department of Physics, University of Florida, Gainesville, FL, USA. *e-mail: luxy@bnu.edu.cn; pdai@rice.edu

Supplemental Material: Anisotropic spin fluctuations in detwinned FeSe

Tong Chen, Youzhe Chen, Andreas Kreisel, Xingye Lu, Astrid Schneidewind, Yiming Qiu,
Jitae Park, Toby G. Perring, Ross Stewart, Huibo Cao, Rui Zhang, Yu Li, Yan Rong,
Yuan Wei, Brian M. Andersen, P. J. Hirschfeld, Collin Broholm, and Pengcheng Dai

I. CALCULATION OF THE SUSCEPTIBILITY USING AN ITINERANT APPROACH

For the theoretical calculations of the spin susceptibility in the normal state and superconducting state, we use a tight-binding parametrization proposed for FeSe earlier[1–4]

$$H = \sum_{\mathbf{k}\sigma\ell\ell'} t_{\mathbf{k}}^{\ell\ell'} c_{\ell\sigma}^\dagger(\mathbf{k}) c_{\ell'\sigma}(\mathbf{k}), \tag{S1}$$

where $c_{\ell\sigma}^\dagger(\mathbf{k})$ is the Fourier amplitude of an operator $c_{i\ell\sigma}^\dagger$ that creates an electron in one of the 5 Fe $3d$ Wannier orbitals ℓ with spin $\sigma \in \{\uparrow, \downarrow\}$ and $t_{\mathbf{k}}^{\ell\ell'}$ is the Fourier transform of the hoppings which are available in the Supplemental Information of Ref. [2]. The kinetic energy also includes an orbital order term in the d_{xz} and d_{yz} orbitals,

$$H_{OO} = \Delta_b \sum_{\mathbf{k}} (\cos k_x - \cos k_y)(n_{xz}(\mathbf{k}) + n_{yz}(\mathbf{k})) + \Delta_s \sum_{\mathbf{k}} (n_{xz}(\mathbf{k}) - n_{yz}(\mathbf{k}))\,, \tag{S2}$$

where $n_\ell(\mathbf{k}) = \sum_\sigma c_{\ell\sigma}^\dagger(\mathbf{k}) c_{\ell\sigma}(\mathbf{k})$, and a component of spin-orbit coupling of type $S^z L^z$.

For later reference, we introduce the unitary transformation with the matrix elements $a_\mu^\ell(\mathbf{k})$ that diagonalizes the Bloch Hamiltonian such that it becomes $H = \sum_{\mathbf{k}\sigma\mu} \tilde{E}_\mu(\mathbf{k}) c_{\mu\sigma}^\dagger(\mathbf{k}) c_{\mu\sigma}(\mathbf{k})$, with eigenenergies $\tilde{E}_\mu(\mathbf{k})$ and the creation operator $c_{\mu\sigma}^\dagger(\mathbf{k})$ for an electron in Bloch state $\mu, \mathbf{k}$. We parametrize the Green's function with a phenomenological ansatz in orbital space as[2–5]

$$\tilde{G}_{\ell\ell'}(\mathbf{k}, \omega_n) = \sqrt{Z_\ell Z_{\ell'}}\ \sum_\mu \frac{a_\mu^\ell(\mathbf{k}) a_\mu^{\ell'*}(\mathbf{k})}{i\omega_n - \tilde{E}_\mu(\mathbf{k})} = \sqrt{Z_\ell Z_{\ell'}}\ \sum_\mu a_\mu^\ell(\mathbf{k}) a_\mu^{\ell'*}(\mathbf{k}) \tilde{G}^\mu(\mathbf{k}, \omega_n), \tag{S3}$$

with quasiparticle weights Z_ℓ in orbital ℓ. We have also introduced the (coherent) Green's function in band space as $\tilde{G}^\mu(\mathbf{k}, \omega_n) = [i\omega_n - \tilde{E}_\mu(\mathbf{k})]^{-1}$. For the calculation of the susceptibility in presence of interactions via a random phase approach (RPA), we include local interactions of the standard Hubbard-Hund Hamiltonian

$$H = U \sum_{i,\ell} n_{i\ell\uparrow} n_{i\ell\downarrow} + U' \sum_{i,\ell'<\ell} n_{i\ell} n_{i\ell'} + J \sum_{i,\ell'<\ell} \sum_{\sigma,\sigma'} c_{i\ell\sigma}^\dagger c_{i\ell'\sigma'}^\dagger c_{i\ell\sigma'} c_{i\ell'\sigma} + J' \sum_{i,\ell'\neq\ell} c_{i\ell\uparrow}^\dagger c_{i\ell\downarrow}^\dagger c_{i\ell'\downarrow} c_{i\ell'\uparrow}, \tag{S4}$$

with the parameters U, U', J, J' that fulfill spin-rotational invariance, i.e. $U' = U - 2J$, $J = J'$ such that there are only two parameters U and J/U left to specify the interactions. These are set to the values as used earlier[3, 4], $U = 0.57\,\mathrm{eV}$ ($U = 0.36\,\mathrm{eV}$ for the fully coherent calculation) and $J/U = 1/6$. Note that our ansatz Eq. (S3) contains a self-energy $\Sigma_{\ell\ell'}(\mathbf{k}, \omega_n)$ that is in principle generated from these interactions, but not calculated self-consistently. The orbital susceptibility in the normal state is renormalized in similar ways

$$\tilde{\chi}^0_{\ell_1\ell_2\ell_3\ell_4}(q) = -\sum_{k,\mu,\nu} \tilde{M}^{\mu\nu}_{\ell_1\ell_2\ell_3\ell_4}(\mathbf{k}, \mathbf{q}) \tilde{G}^\mu(k+q) \tilde{G}^\nu(k), \tag{S5}$$

where we have adopted the shorthand $k \equiv (\mathbf{k}, \omega_n)$ and defined

$$\tilde{M}^{\mu\nu}_{\ell_1\ell_2\ell_3\ell_4}(\mathbf{k}, \mathbf{q}) = \sqrt{Z_{\ell_1} Z_{\ell_2} Z_{\ell_3} Z_{\ell_4}} a_\nu^{\ell_4}(\mathbf{k}) a_\nu^{\ell_2,*}(\mathbf{k}) a_\mu^{\ell_1}(\mathbf{k}+\mathbf{q}) a_\mu^{\ell_3,*}(\mathbf{k}+\mathbf{q}). \tag{S6}$$

containing the orbital to band matrix elements a_ν^ℓ. Next, the internal frequency summation is done analytically and the susceptibility $\tilde{\chi}^0_{\ell_1\ell_2\ell_3\ell_4}$ is obtained by integrating over the full Brillouin zone. This calculation is identical to first calculating $\chi^0_{\ell_1\ell_2\ell_3\ell_4}$ using a fully coherent Green's function and then relating the two quantities via

$$\tilde{\chi}^0_{\ell_1\ell_2\ell_3\ell_4}(\mathbf{q}) = \sqrt{Z_{\ell_1} Z_{\ell_2} Z_{\ell_3} Z_{\ell_4}}\ \chi^0_{\ell_1\ell_2\ell_3\ell_4}(\mathbf{q}), \tag{S7}$$

i.e. the quasiparticle weights just enter as prefactors.

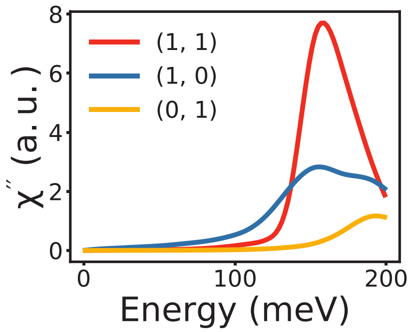

FIG. S1. Dynamical susceptibility in the normal state as calculated from Eq. (S8). At low energies, the $(1,0)$ fluctuations dominate, see also Fig. 5 in the main text, while at higher energies Néel fluctuations at $(1,1)$ set in and beome domiant.

The resulting bare susceptibility in the fully coherent case has overall similar magnitudes in the three channels with $\mathbf{q}=(\pi,\pi)$, $\mathbf{q}=(\pi,0)$ and $\mathbf{q}=(0,\pi)$, see Fig. 5 of the main text. This can be attributed to the three nesting conditions at low energies between the Fermi surface pockets; additionally the channels are dominated by the d_{xy} orbital component for $\mathbf{q}=(\pi,\pi)$, the d_{xz} orbital component for $\mathbf{q}=(0,\pi)$ and the d_{yz} orbital component for $\mathbf{q}=(\pi,0)$[3, 4]. Taking into account the quasiparticle weights which we fix to $\{\sqrt{Z_l}\}=[0.2715,0.9717,0.4048,0.9236,0.5916]$[2, 3, 5], it is easy to understand that the $\mathbf{q}=(\pi,\pi)$ and $\mathbf{q}=(0,\pi)$ channels of the bare susceptibility will be suppressed, such that the physical spin susceptibility has dominant low-energy weight at $(\pi,0)$. The actual numbers for Z_l employed do not change these results qualitatively as long as the structure $Z_{xy}<Z_{xz}<Z_{yz}$ is kept[4, 5]. The interactions as written in Eq. (S4) are incorporated into the two-particle properties via the random-phase approximation (RPA) such that the spin-fluctuation part of the RPA susceptibility, $\tilde{\chi}_1^{\mathrm{RPA}}$, is given as

$$\tilde{\chi}^{\mathrm{RPA}}_{1\,\ell_1\ell_2\ell_3\ell_4}(\mathbf{q},\omega)=\left\{\tilde{\chi}^0(\mathbf{q},\omega)\left[1-\bar{U}^s\tilde{\chi}^0(\mathbf{q},\omega)\right]^{-1}\right\}_{\ell_1\ell_2\ell_3\ell_4}, \tag{S8}$$

where $\bar{U}^s$ is an interaction matrix containing the coupling constants U,U',J,J' of as defined in Eq. (S4). To compare to experimental investigations, we calculate the total physical spin susceptibility,

$$\chi(\mathbf{q},\omega)=\frac{1}{2}\sum_{\ell\ell'}\tilde{\chi}^{\mathrm{RPA}}_{1\,\ell\ell'\ell'}(\mathbf{q},\omega)=\sum_{\ell}\chi_\ell(\mathbf{q},\omega)\,. \tag{S9}$$

Results for the total susceptibility for the orbital selective case are shown in Fig. S1 where the imaginary part $\chi''(\mathbf{q},\omega)$ is plotted as function of energy for three different momentum transfers. At low energies (see Fig. 5 in the main text), the susceptibility at $(1,0)$ is largest, but at higher energies scattering processes play a role that also yield significant weight at $(1,1)$. To break down contributions from individual orbitals, we plot $\chi_\ell(\mathbf{q},\omega)$ in Fig. 5(h) of the main text.

Spin excitations in the normal state The dynamic structure factor

$$S(\mathbf{q},\omega)=\frac{1}{1-e^{-\omega/T}}f^2(\mathbf{q})\,\mathrm{Im}\,\chi_{\mathrm{RPA}}(\mathbf{q},\omega) \tag{S10}$$

is directly proportional to the measured intensity in INS experiments. For its calculation we multiply with the Bose factor and the magnetic form factor[6] $f(\mathbf{q})$ of Fe^{2+}.

Response in the superconducting state For the calculations in the superconducting state, we impose an order parameter that is diagonal in band space $\Delta_\mu(\mathbf{k})$ and has been calculated earlier[3] in terms of a symmetry function $g(\mathbf{k})$ on the Fermi surface. Next, we obtain the eigenenergies of the Bogoliubov quasiparticles $\epsilon_\mu(\mathbf{k})=\sqrt{\tilde{E}_\mu(\mathbf{k})^2+\Delta_\mu(\mathbf{k})^2}$. The susceptibility tensor then reads[7]

$$\tilde{\chi}^0_{\ell_1\ell_2\ell_3\ell_4}(q)=-\sum_{k,\mu,\nu}\tilde{M}^{\mu\nu}_{\ell_1\ell_2\ell_3\ell_4}(\mathbf{k},\mathbf{q})[G^\mu_{\mathrm{BCS}}(k+q)G^\nu_{\mathrm{BCS}}(k)+F^\mu_{\mathrm{BCS}}(k+q)F^\nu_{\mathrm{BCS}}(-k)], \tag{S11}$$

with the normal Green's function $G^\mu_{\mathrm{BCS}}(k)$ and the anomalous Green's function $F^\mu_{\mathrm{BCS}}(k)$ given by

$$G^\mu_{\mathrm{BCS}}(k)=\frac{i\omega_n+\tilde{E}_\mu(\mathbf{k})}{\omega_n^2+\epsilon_\mu(\mathbf{k})^2},\qquad F^\mu_{\mathrm{BCS}}(k)=\frac{\Delta_\mu(\mathbf{k})}{\omega_n^2+\epsilon_\mu(\mathbf{k})^2}\,. \tag{S12}$$

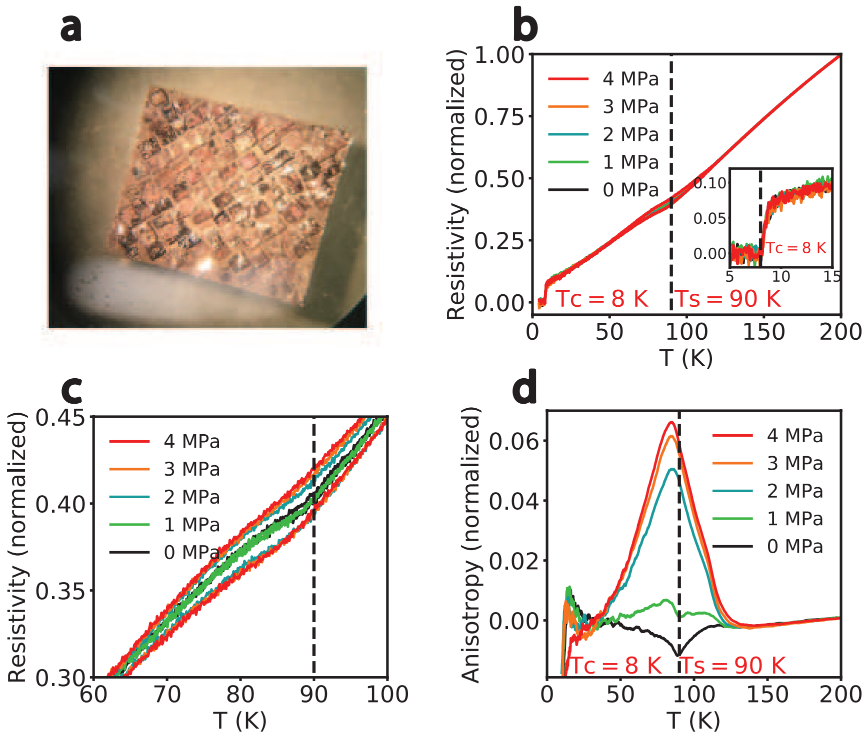

FIG. S2. (a) A photograph of many single crystals of FeSe glued on one $BaFe_2As_2$ single crystal. (b) Temperature dependence of the resistivity of one FeSe crystal as a function of uniaxial pressure on $BaFe_2As_2$ measured using the Montgomery method as in earlier work [10]. The resistivity data at 200 K are normalized to 1. The vertical dashed line marks $T_s = 90$ K. T_c of 8 K is seen in the data as well. (c) Expanded view of panel (b) near T_s. (d) Temperature dependence of the resistivity anisotropy of FeSe as estimated from the Montgomery method. Resistivity anisotropy is defined as $(\rho_{a_o} - \rho_{b_o})/(\rho_{a_o} + \rho_{b_o})$, where ρ_{a_o} and ρ_{b_o} are the resistivity along the a_o and b_o axis of the orthorhombic lattice, respectively [10].

II. SAMPLE AND NEUTRON SCATTERING EXPERIMENT

Single crystal growth method and transport measurements. The high quality FeSe single crystals used in the experiments are grown by a chemical vapor transport method. Fe and Se powder are sealed in quartz tubes with KCl-$AlCl_3$ flux. The growth takes 28 days in a temperature gradient from 330°C to 400°C. Typical samples are 1×1 mm^2 in area and < 0.1 mm in thickness. The square-shaped $BaFe_2As_2$ crystals are aligned using a Laue camera and cut along the tetragonal $[1, 1, 0]$ and $[1, -1, 0]$ directions by a high-precision wire saw. Since single crystals of FeSe have one natural edge 45° rotated from the orthorhombic a_o direction, we can use an optical method to co-align FeSe on the surface of $BaFe_2As_2$. Given our intent to measure spin excitations in detwinned FeSe, we aligned and glued (with CYTOP type-M) about 300 small pieces FeSe single crystals on many pieces of big $BaFe_2As_2$ single crystals [Fig. S2(a)]. CYTOP is a hydrogen free polymer that have been used as glue by many neutron scattering groups to avoid the large incoherent scattering from hydrogen in regular glue. According to manufacturer (http://www.bellexinternational.com/products/cytop/pdf/cytop-catalog-p8.pdf), CYTOP has tensile strength of 41-49 MPa, tensile extension ratio of 162-192 %, yield strength of 40 MPa, and tensile modulus of 1400-1600 MPa at 25°C. In our experiments, we applied a very thin layer (on the order several μm) of CYTOP and dried it in a hotplate set at 100°C. Although we do not know the mechanical properties of CYTOP at low-temperatures, our experiments reveal that it worked very well in detwinning the FeSe. Fig. S2(b) shows the temperature dependence of the resistivity of one FeSe crystal as a function of uniaxial pressure applied to $BaFe_2As_2$. Consistent with earlier work on uniaxial pressure detwinned FeSe using a mechanical device [8], we find that gluing FeSe on $BaFe_2As_2$ works equally well [Figs. S2(c) and (d)].

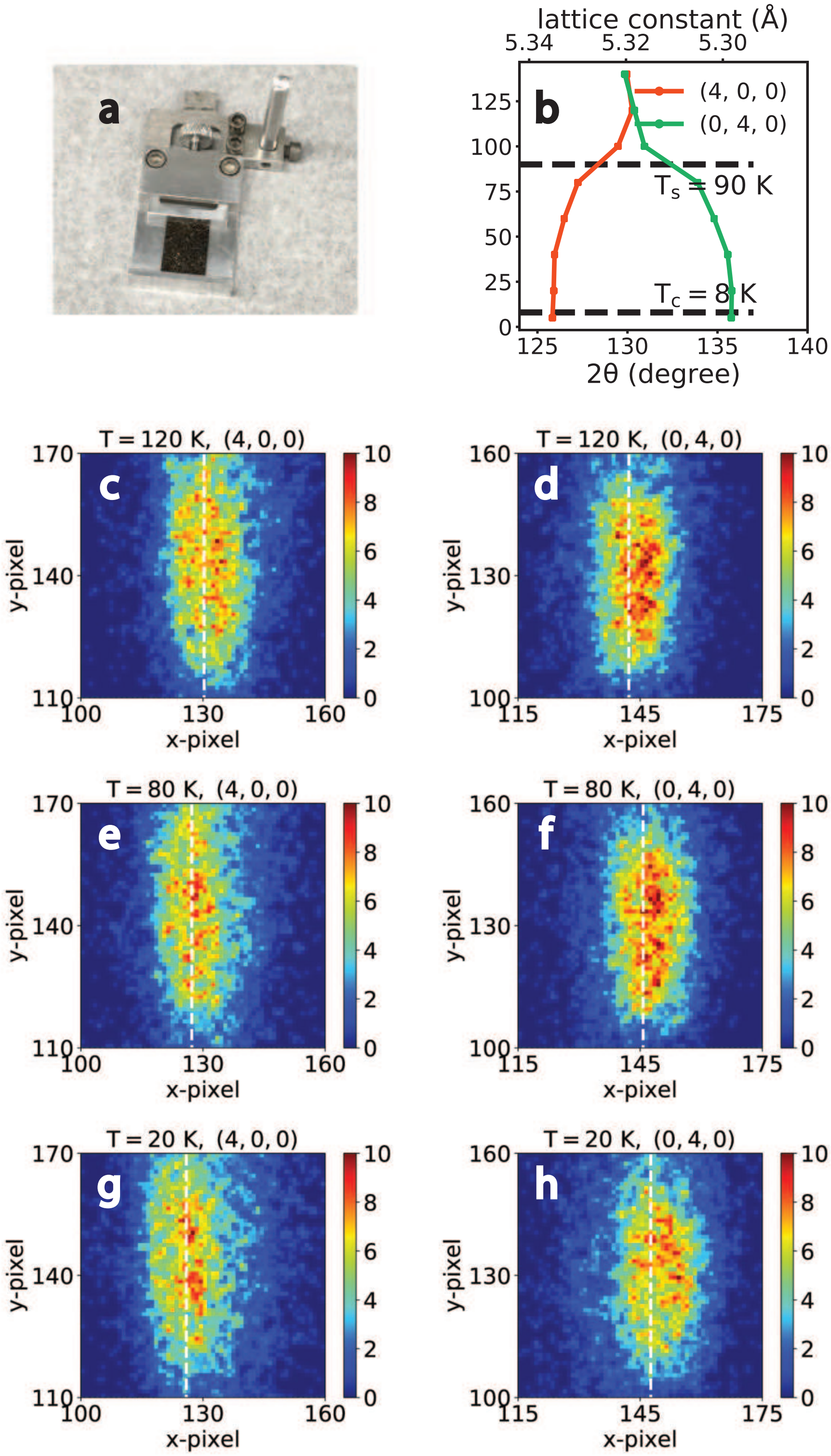

FIG. S3. (a) FeSe samples on a single piece of $BaFe_2As_2$ mounted on a detwinned device. Uniaxial pressure is applied by turning the aluminum screw. (b) Temperature dependence of lattice constant calculated from positions of nuclear $(4, 0, 0)$ and $(0, 4, 0)$ Bragg peaks. (c-h) Temperature dependence of the $(4, 0, 0)$ and $(0, 4, 0)$ Bragg peak intensity and position. The data are taken on HB-3A on a single piece of $BaFe_2As_2$ with many FeSe single crystals as shown in Fig. S2(a).

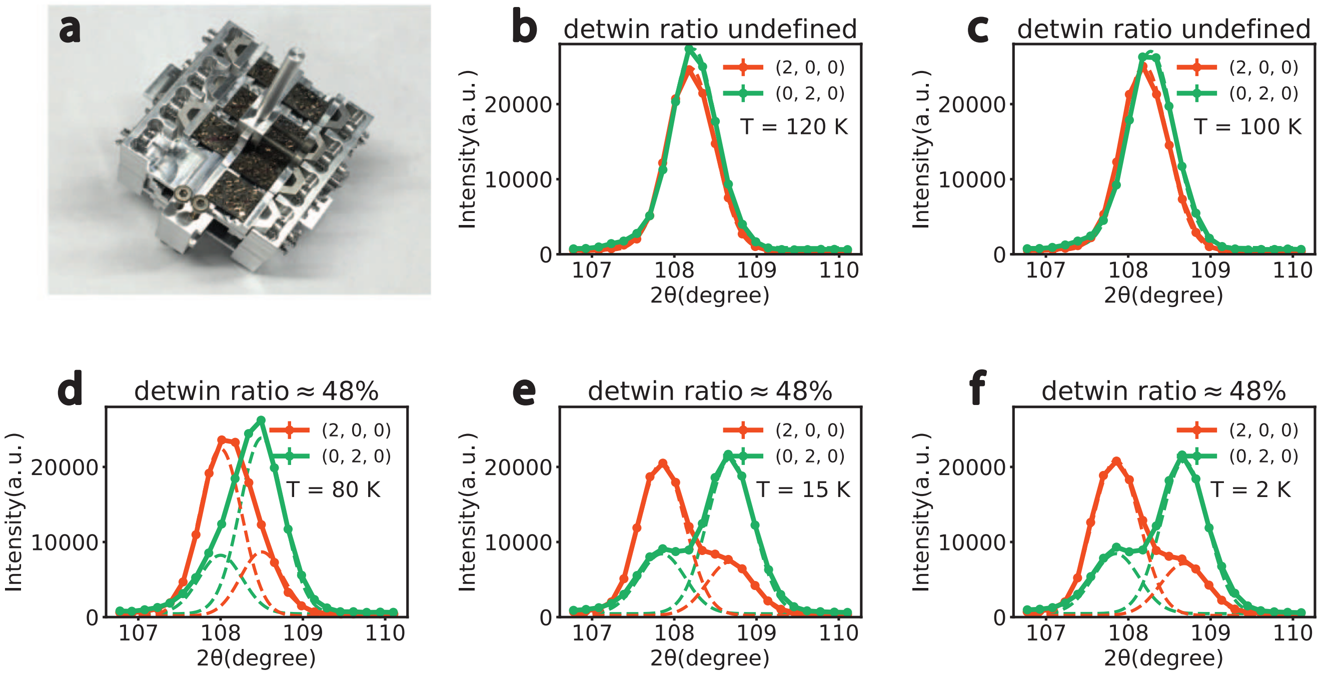

FIG. S4. (a) The mechanical device used to simultaneously detwin at most 32 pieces of large $BaFe_2As_2$ single crystals with FeSe glued on top. Measurements of the nuclear Bragg peak $(2,0,0)$ and $(0,2,0)$ at (b) 120 K ($> T_s = 90$ K), (c) 100 K, (d) 80 K, (e) 15 K, (f) 2 K in the assembly of the samples on PANDA. The intensity differences of the double peaks seen in the data reveal the actual detwinning ratio of FeSe.

Elastic neutron scattering experimental details. Elastic neutron experiments were carried out on the HB-3A four-Circle diffractometer at the High-Flux-Isotope Reactor (HFIR), Oak Ridge National Laboratory (ORNL), United States to first check if the method works well in detwinning FeSe on a single piece of $BaFe_2As_2$ [Fig. S2(a)]. HB-3A uses a silicon monochromator and a scintillator-based 2D Anger Camera. To detwin FeSe, we apply uniaxial pressure on one single crystal $BaFe_2As_2$ sample as shown in Fig. S3(a). Figs. S3(c)-(h) show temperature dependence of nuclear $(4,0,0)$ and $(0,4,0)$ Bragg peaks of FeSe, which reveal clear shift, instead of splitting, of the nuclear Bragg peaks below T_s. The lattice constants can be calculated from the position of the Bragg peak center at each temperature [Fig. S3(b)], which also indicate that the FeSe samples on a single piece of $BaFe_2As_2$ are essentially fully detwinned. However, to carry out inelastic neutron scattering measurements, we will need many $BaFe_2As_2$ crystals with FeSe glued on top to increase scattering intensity from detwinned FeSe. For this reason, we designed and built a multi sample holder as shown in Fig. S4(a), which can detwin up to 32 $BaFe_2As_2$ single crystals with FeSe on top simultaneously. However, the detwinning ratio for all FeSe crystals for the actual assembly is considerably reduced as shown in Fig. 1(e) of the main text.

Inelastic neutron scattering experimental details. Our inelastic neutron scattering experiments on twinned samples were done on MACS cold triple axis spectrometer at NIST center for neutron scattering at Gaithersburg, Maryland. MACS spectrometer has a double focusing pyrolytic graphite [PG(002)] monochoromator and multi detectors. We used $E_f = 3.7$ meV with a BeO filter after the sample and a Be filter before the monochromator for energy transfers below $E = 1.5$ meV.

Our inelastic neutron scattering experiments on detwinned samples were carried out on the PANDA cold neutron and PUMA thermal neutron triple-axis spectrometers, at Forschungs-Neutronenquelle Heinz Maier-Leibnitz (MLZ), Garching, Germany, and on the MAPS time-of-flight chopper spectrometer, at ISIS, Rutherford-Appleton laboratory, Didcot, United Kingdom [9].

For PANDA experiments, a double-focused pyrolytic graphite [PG(002)] monochromator and analyzer with fixed scattered neutron energy $E_f = 5.1$ meV were used with collimations of none-40′-40′-none for inelastic measurements. For elastic measurements, we used $E_f = 4.39$ meV with collimations of 80′-80′-80′-80′. For thermal neutron measurements on PUMA, we used $E_f = 14.69$ meV with double focusing monochromator and analyzer and no collimators. For MAPS neutron time-of-flight measurements, we used an incident beam energy of $E_i = 38$ meV with the incident beam along the c-axis of the crystal.

Fig. S2(a) shows a picture of the assembly of FeSe samples on $BaFe_2As_2$ substrates used for inelastic neutron

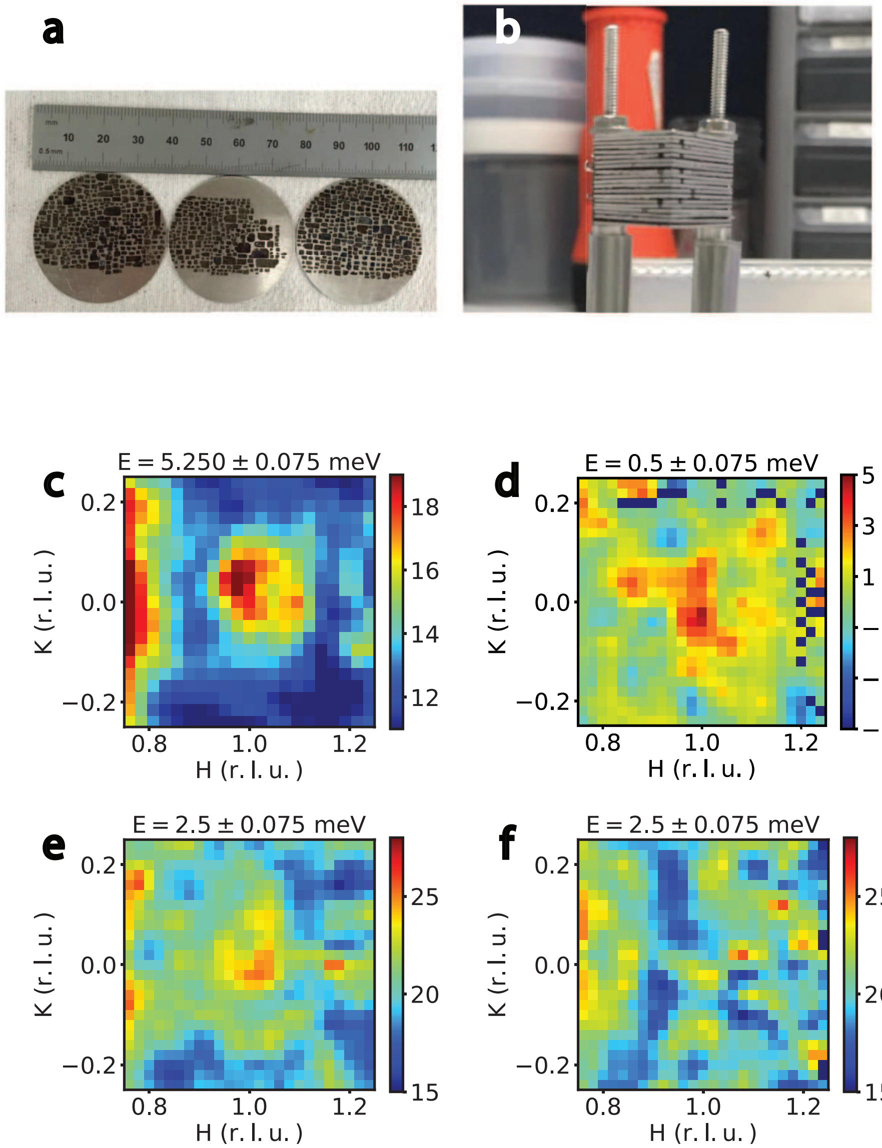

FIG. S5. (a) A picture of the FeSe single crystals glued on aluminum plates for experiments on twinned samples on MACS. The ruler scale is in mm. (b) Crystal assembly cut to fit the cryostat on MACS. (c) Incommensurate spin fluctuations at $E = 5.25 \pm 0.075$ meV observed at MACS at $T = 10$ K. These are raw data for Fig. 2(h) of the main text, but at $T = 2$ K. (d) Commensurate spin fluctuations at $E = 0.5 \pm 0.075$ meV at $T = 10$ K. (e) Normal state ($T = 10$ K) spin fluctuations at $E = 2.5 \pm 0.075$ meV are commensurate near $(1, 0)$. (f) Identical scan in the superconducting state ($T = 2$ K) at $E = 2.5 \pm 0.075$ meV, the highest energy where a spin gap opens and normal state spin fluctuations are suppressed.

scattering experiments described in the main text. Fig. S3(a) shows one piece of $BaFe_2As_2$ with many FeSe single crystals mounted in a single detwinning device. The uniaxial pressure applied was sufficient to completely detwin $BaFe_2As_2$, as seen from inelastic neutron scattering measurements of spin waves from $BaFe_2As_2$. This means the applied pressure is above 12 MPa [9]. Using this device, we studied the temperature dependence of the nuclear $(4, 0, 0)$ and $(0, 4, 0)$ Bragg peaks of FeSe on HB-3A. In the tetragonal state above T_s, $(4, 0, 0)$ and $(0, 4, 0)$ peaks occur at the same 2θ angle, as we find in Fig. S3(b). On cooling below T_s, we see clear shifting of the peak positions indicating essentially 100% detwinning around $T = 20$ K [Figs. S3(g) and (h)].

Fig. S4(a) shows a picture of the actual sample assembly for FeSe on multiply $BaFe_2As_2$ single crystals used in our inelastic neutron scattering experiments. With this assembly, the detwinned FeSe can be aligned in the $(H, K, 0)$ scattering plane for triple axis experiments and in the $(H, 0, L)$ scattering plane for MAPS measurements. Figs. S4(b)-(f) plot the temperature dependence of the nuclear $(2, 0, 0)$ and $(0, 2, 0)$ Bragg peaks scanned along the $[H, 0, 0]$ and $[0, K, 0]$ directions on PANDA. From the splitting of the $(2, 0, 0)$ and $(0, 2, 0)$ Bragg peaks below T_s, we can accurately

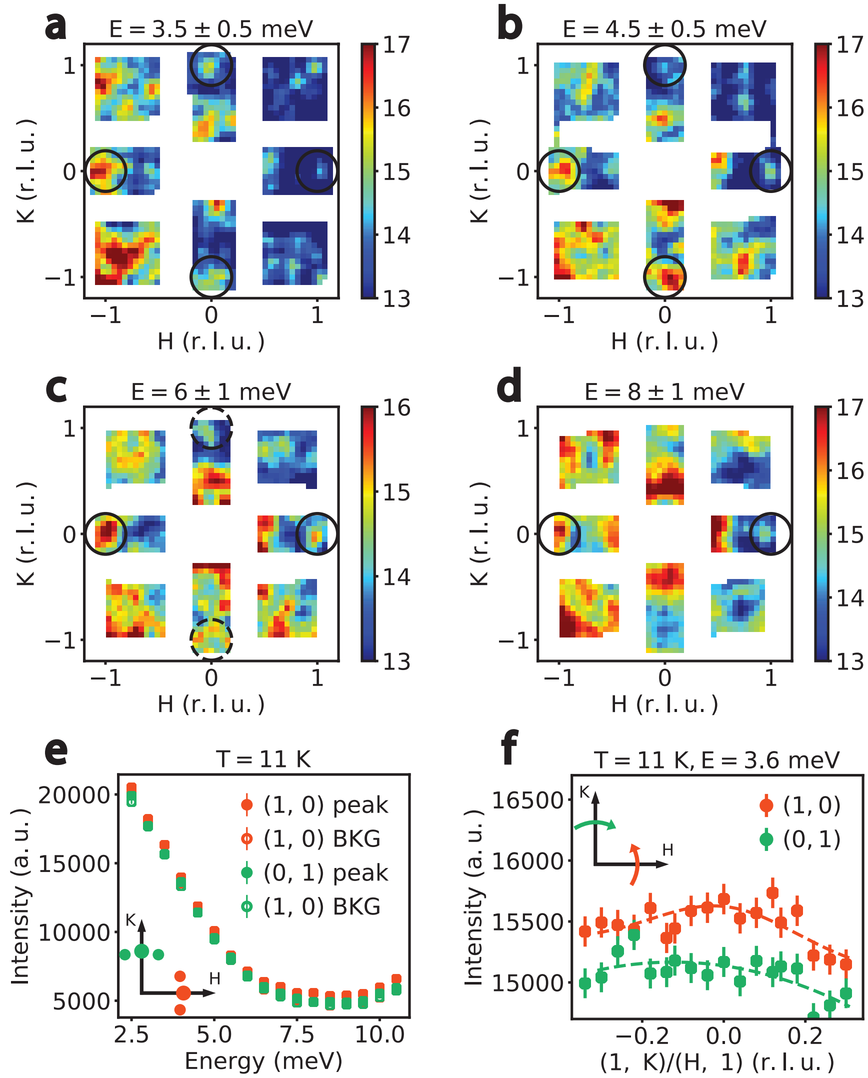

FIG. S6. Images of spin fluctuations taken on MAPS using partially detwinned FeSe on multiply $BaFe_2As_2$ single crystals. Raw data at energies of (a) $E = 3.5 \pm 0.5$ meV, (b) 4.5 ± 0.5 meV, (c) 6 ± 1 meV, and (d) 8 ± 1 meV. Black circles mark positions of expected spin fluctuations. (e) raw data of energy scans on detwinned FeSe at $(1, 0)$, $(0, 1)$, and corresponding background positions taken on PUMA. The positions of background scattering are marked as smaller solid circles in the inset. (f) Raw data of transverse scans at $E = 3.6$ meV taken on PUMA. No clear peaks are seen at expected positions due to high background scattering.

estimate the detwinning ratio of the system. Given the observed Bragg peaks at $(2, 0, 0)$ and $(0, 2, 0)$ have $I(2, 0, 0)_o$ and $I(0, 2, 0)_o$ (the intensity of the green dashed curve at the same 2θ angle as the red solid curve around 107.8 degrees) intensity, respectively. Then the detwinning ratio η is $\eta = (I(2, 0, 0)_o - I(0, 2, 0)_o)/(I(2, 0, 0)_o + I(0, 2, 0)_o) \approx 50\%$ at $T = 2$ K [10]. If we assume that the volume fraction of the $(2, 0, 0)$ domain is α, we would have $I(2, 0, 0)_o \approx \alpha I(2, 0, 0)$ since $(0, 2, 0)$ peak occurs at a slightly different angle [Fig. S4(f)]. For a 100% detwinned sample, $\alpha = 1$ and $I(2, 0, 0)_o \approx \alpha I(2, 0, 0)$. For a partially detwinned sample, we have $I(0, 2, 0)_o \approx (1 - \alpha)I(0, 2, 0)$, and therefore $\alpha = (\eta + 1)/2$. For spin excitations in a partially detwinned FeSe, we define the intrinsic magnetic scattering in 100% detwinned FeSe at wave vectors $\mathbf{Q}_{\rm AF} \approx (\pm 1, 0)$ and $(0, 1)$ to be $S(\mathbf{Q}_{\rm AF}, E)_i$ and $S(\mathbf{Q} = (0, 1), E)_i$, respectively. Since the scattering at $\mathbf{Q} = (0, 1)$ may be finite for a 100% detwinned FeSe, the observed intensity at $\mathbf{Q}_{\rm AF}$ and $(0, 1)$ can be written as: $S(\mathbf{Q}_{\rm AF}, E) = \alpha S(\mathbf{Q}_{\rm AF}, E)_i + (1 - \alpha)S(\mathbf{Q} = (0, 1), E)_i$, and $S(\mathbf{Q} = (0, 1), E) = \alpha S(\mathbf{Q} = (0, 1), E)_i + (1 - \alpha)S(\mathbf{Q}_{\rm AF}, E)_i$, where $S(\mathbf{Q}_{\rm AF}, E)_i$ and $S(\mathbf{Q} = (0, 1), E)_i$ are intrinsic magnetic scattering of 100% detwinned FeSe. Since $\alpha \approx 0.75$, the observed intensity at $S(\mathbf{Q}_{\rm AF}, E)$ and $S(\mathbf{Q} = (0, 1), E)$ are known, we find $S(\mathbf{Q}_{\rm AF}, E)_i = [(1 - \alpha)S(\mathbf{Q} = (0, 1), E) - \alpha S(\mathbf{Q}_{\rm AF}, E)]/(1 - 2\alpha)$ and $S(\mathbf{Q} = (0, 1), E)_i = [(1 - \alpha)S(\mathbf{Q}_{\rm AF}, E) - \alpha S(\mathbf{Q} = (0, 1), E)]/(1 - 2\alpha)$. Figs. 4(e) and 4(f) in the main text show the corrected intrinsic $S(\mathbf{Q}_{\rm AF}, E)_i$ and $S(\mathbf{Q} = (0, 1), E)_i$

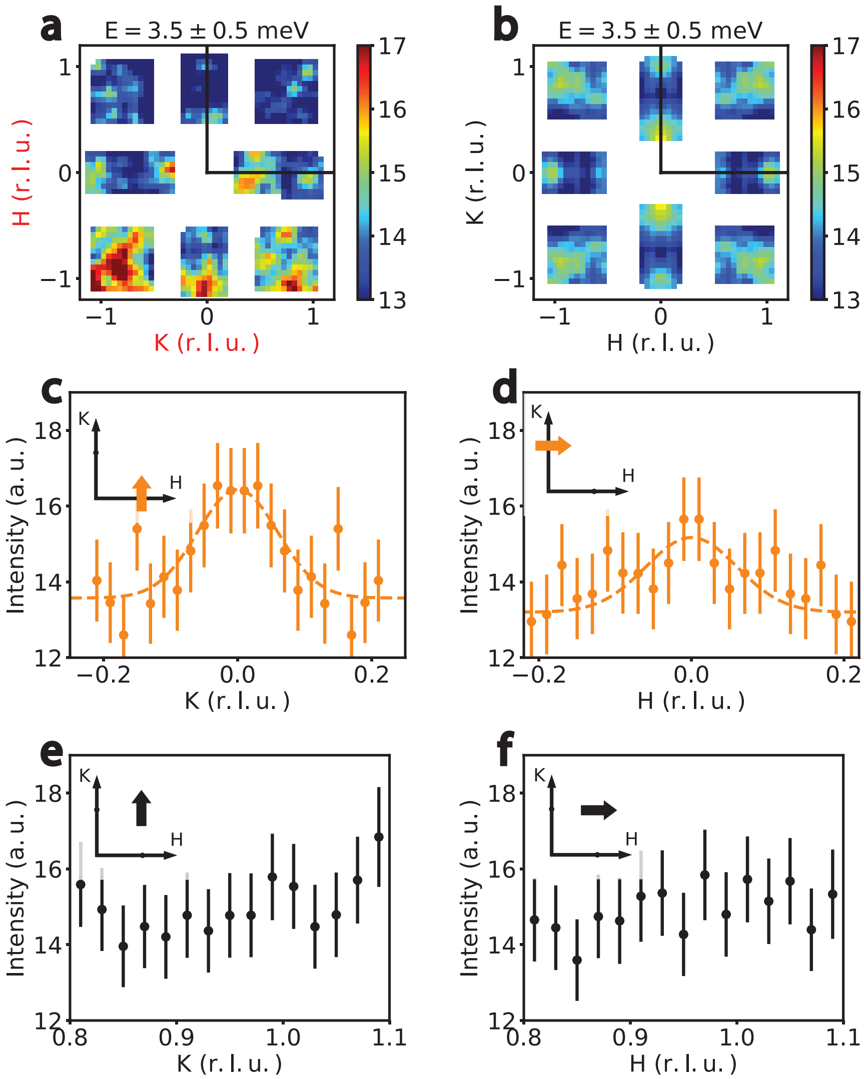

FIG. S7. (a) Images of spin fluctuations at $E = 3.5 \pm 0.5$ meV and (b) the folded data data to improve statistics in the normal state. (c,d) Cuts along the wave vector $(1, K)$ and $(H, 1)$ directions, respectively. (e,f) Cuts along the $(1, 1)$ direction show no evidence of magnetic scattering. The high intensity near these wave vectors in the data are background scattering.

for 100% detwinned FeSe. When $S(\mathbf{Q}_{\rm AF}, E) \approx S(\mathbf{Q} = (0, 1), E)$, magnetic fluctuations follow C_4 rotational symmetry regardless of the value α. This means that the scattering around 3 meV must have finite value at $S(\mathbf{Q} = (0, 1), E)_i$, suggesting that the detwinned FeSe has approximate C_4 symmetry around this energy.

To understand the effect of detwinned FeSe, we must first determine the temperature dependence of the magnetic scattering in twinned FeSe. Figs. S5(a) and (b) show pictures of our twinned FeSe glued on thin aluminum plates. The experiments are carried out at MACS. Fig. S5(c) shows raw data of Fig. 2(h), which has ring-like magnetic scattering around $E = 5.25 \pm 0.075$ meV in the superconducting state. Fig. S5(d) shows scattering at $E = 0.5$ meV, where the low-temperature ($T = 2$ K) background scattering was subtracted. To demonstrate the presence of a superconductivity-induced spin gap, we show images of magnetic scattering at $E = 2.5 \pm 0.075$ meV above [Fig. S5(e)] and below [Fig. S5(f)] T_c.

Figs. S6(a)-(d) show raw data images of spin excitations of detwinned FeSe at $E = 3.5 \pm 0.5$, 4.5 ± 0.5, 6 ± 1, and 8 ± 1 meV, respectively, obtained on MAPS. At all energies probed, we find scattering near the commensurate wave vectors $(1, 0), (-1, 0), (0, 1)$, and $(0, -1)$, indicating that the signal is magnetic in origin. At energies of $E = 3.5 \pm 0.5$ and 4.5 ± 0.5 meV, spin excitations at $(1, 0)$ and $(0, 1)$ have similar intensity, whereas the scattering intensity at $(1, 0)$ is considerably higher than that of $(0, 1)$ at $E = 6 \pm 1$, and 8 ± 1 meV. On the other hand, while we find clear scattering near the commensurate wave vectors $(-1, -1)$ and $(1, 1)$ at $E = 3.5 \pm 0.5$ meV in Fig. S6(a), there are no

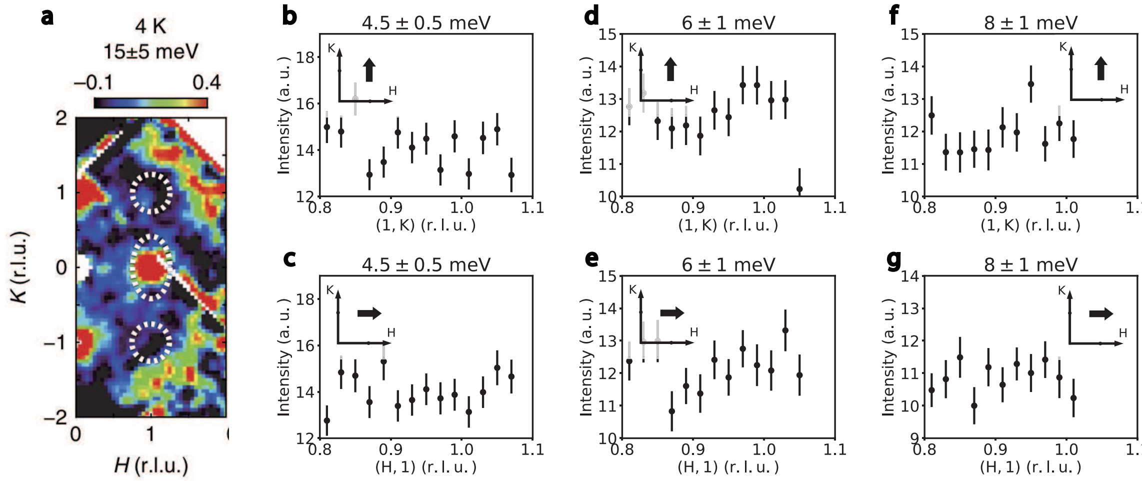

FIG. S8. (a) Images of spin fluctuations at $E = 15 \pm 5$ meV and $T = 4$ K obtained from the twinned FeSe in Ref. [12]. There is no evidence of magnetic scattering at $(1, 1)$ in the superconducting state. (b,d,f) Cuts of the folded two-dimensional scattering along the wave vector $(1, K)$ direction at energies of $E = 4.5 \pm 0.5, 6 \pm 1, 8 \pm 1$ meV. (c,e,g) Cuts along the wave vector $(H, 1)$ direction. We see no evidence of magnetic scattering around $(1, 1)$ in the normal state at 12 K.

scattering centered at the commensurate wave vectors $(-1, 1)$ and $(1, -1)$, thus suggesting that the scattering near $(-1, -1)$ and $(1, 1)$ is spurious in origin. This identification is supported by data in Figs. S6(b)-(d), where we find no commensurate scattering near $(1, 1), (-1, -1), (-1, 1)$, and $(1, -1)$ at $E = 4.5 \pm 0.5$, 6 ± 1, and 8 ± 1 meV.

Figs. S6(e),(f) show raw data for energy and wave vectors scans obtained on PUMA at 11 K. In the experimental setup for PUMA and PANDA, the crystallographic c-axis is perpendicular to the scattering plane, meaning that we are probing spin excitations of FeSe with $L = 0$. In this experimental geometry, the spin gap from the $BaFe_2As_2$ substrate is about 15 meV [11]. This means that the scattering we see up to 11 meV in the PUMA data is likely to be magnetic in origin. For energies below $E = 4$ meV, background scattering makes it difficult to accurately determine the intrinsic magnetic intensity at $(1, 0)$ and $(0, 1)$.

To further determine if the scattering near $(1, 1)$ seen in Fig. 3(a)-3(d) of the main text and Fig. S6 is magnetic in origin, we consider measurements on a twinned sample. From previous inelastic neutron scattering work, it is known that there is a large spin gap at $(1, 1)$ below about $E = 30$ meV in the superconducting state at 4 K [12]. From temperature dependence of the $E = 45 \pm 5$ meV scattering at $(1, 1)$ and $(1, 0)$ in Fig. 4(d) of Ref. [12], we know that the large spin gap at $(1, 1)$ does not change appreciably across T_c. Figs. S7(a) and (b) show unfolded and folded data at $E = 3.5 \pm 0.5$ meV, respectively, for a detwinned sample. Figs. S7(c) and (d) plot cuts along the expected magnetic signal positions at $(1, 0)$, and $(0, 1)$, respectively. The data reveal a clear signal at both wave vectors similar to the triple-axis data on PANDA shown in Fig. 4 of the main text. Similar cuts around the $(1, 1)$ wave vector yielded no peak, consistent with no magnetic scattering at this wave vector [Figs. S7(e),(f)].

Figure S8(a) shows the constant-energy image of the scattering for $E = 15 \pm 5$ at 4 K for twinned FeSe from Ref. [12]. While magnetic scattering is clearly seen at the AF wave vector $(1, 0)$, there is no evidence of magnetic scattering at $(1, \pm 1)$ in the data. Figures S8(b),(d),(f) show constant-energy cuts along the $(1, K)$ direction for our data in Figs. S6(b),(c),(d), respectively. Figures S8(c),(e),(g) show cuts along the $(H, 1)$ direction across the $(1, 1)$ positions for the same energies. By comparing these figures, we conclude that there is no evidence of magnetic scattering below $E = 8 \pm 1$ meV around $(1, 1)$, consistent with the conclusion of Ref. [12] and our own data in Fig. S6(a)-(d).

Fig. S9 shows the raw data of the constant-energy and wave vector scans obtained on PANDA. Figs. S9(a) and (b) show constant energy scans at wave vectors $(1, 0)$ and $(0, 1)$ below and above T_c. The temperature difference plots show a clear resonance at $(1, 0)$ but the scattering at $(0, 1)$ show no variation with temperature across T_c. Since our unpolarized neutron scattering data indicate the presence of a clear superconductivity-induced spin gap below about $E = 2.5$ meV, this means the scattering at $(0, 1)$ in the detwinned sample has a spin gap in the normal state, as otherwise we would expect a negative value in the temperature difference plot in Fig. 4(b). The presence of normal state magnetic scattering at wave vectors $(1, 0)$ and $(0, 1)$ in the detwinned sample is shown in Figs. 3 and 4 of the main text. Figs. S6(c) and (d) show wave vector scans along the $[H, 0, 0]$ and $[0, K, 0]$ directions at $E = 4.0$ meV. Consistent with data in Fig. 4 of the main text, we see that the normal state scattering at $(1, 0)$ and $(0, 1)$ wave vectors has similar intensity. Figs. S6(e) and (f) show background subtracted data.

Finally, we discuss the procedure used to estimate the schematic Figs. 1(f) and 1(g) in the main text. Since data

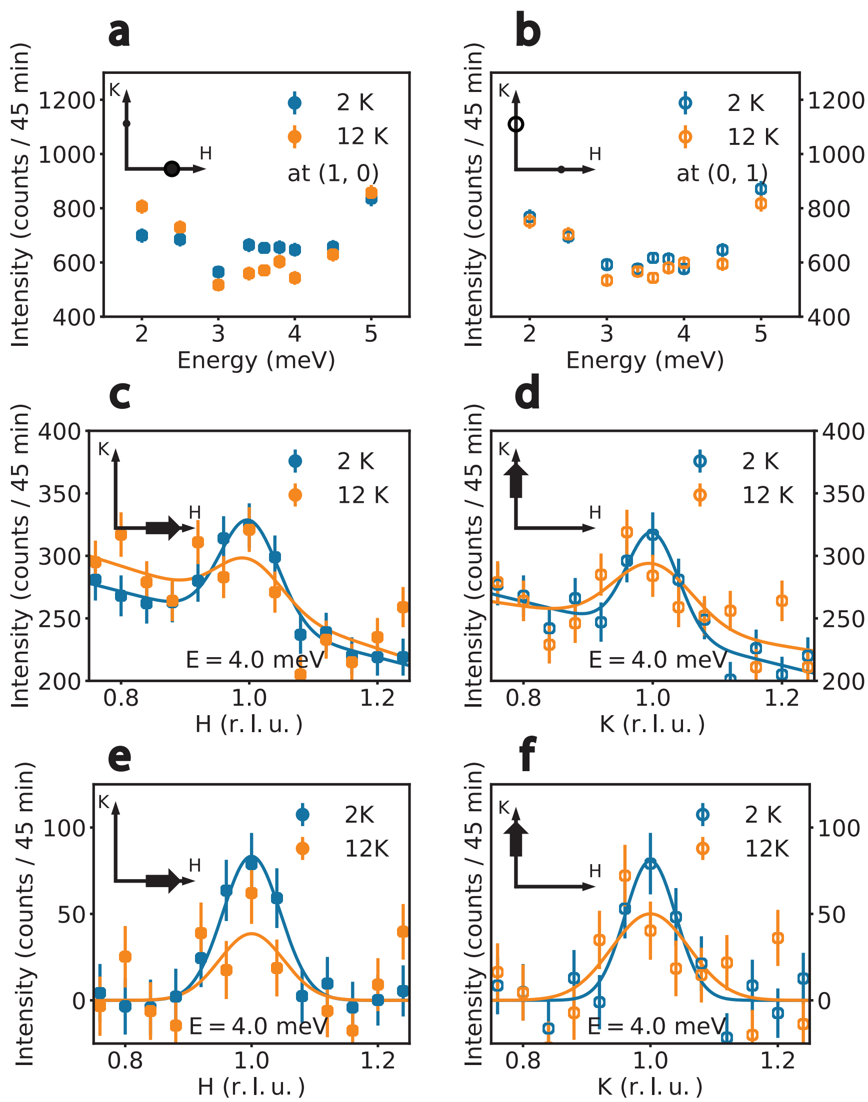

FIG. S9. Constant wave vector scans at (a) $(1,0)$ and (b) $(0,1)$ above and below T_c on the detwinned FeSe obtained on PANDA. These are raw data, and temperature difference plots are shown in Fig. 4 of the main text. (c,d) Constant-energy scans along the $[H,0,0]$ and $[0,K,0]$ directions at $E = 4.0$ meV below and above T_c. The dashed lines are Gaussian fits on a linear background. (e,f) Background subtracted data.

obtained on partially detwinned sample in Figs. 3 and 4 are not as high statistics as those for twinned sample on MACS shown in Fig. 2, we will use MACS data as the basis to estimate the energy dependence of the intensities in a fully detwined FeSe. The strongest evidence for the presence of a C_4 component is from constant-energy scans at $E = 3.6$ meV shown in Figs. 4(c) and 4(d) of the main text. From the detwinning ratio corrected data in Figs. 4(e) and 4(f) of the main text we can estimate the ratio of the $(1,0)$ and $(0,1)$ scattering in the normal state of a fully detwinned sample. The differences scattering between $(1,0)$ and $(0,1)$ is the C_2 component, or magnetic anisotropy, which is about 20% of the total magnetic scattering at $E = 3.6$ meV in the normal state. If we assume the same intensity anisotropy ratio in better statistics data of twinned sample, we can mark it as C_2 in Fig. S10(a). Since Figs. 3(e) and 3(f) of the main text reveal that the magnetic scattering above 8 meV is mostly centered at $(1,0)$ with very small component at $(0,1)$ after the detwinning ratio correction, we can estimate the C_2 component in the normal state as a function of increasing energy. If we assume that the C_2 component monotonically increases with increasing energy and will dominate the scattering above 8 meV, we can fit a function proportional to x^3 across the C_2 intensity at $E = 3.6$ meV as shown in the solid black line of Fig. S10(b).

Since the C_2 component is the difference between $(1,0)$ and $(0,1)$, we can derive the $(1,0)$ and $(0,1)$ scattering if we assume that their sum divided by 2 must equal to measured scattering intensity for a twinned sample. Figure

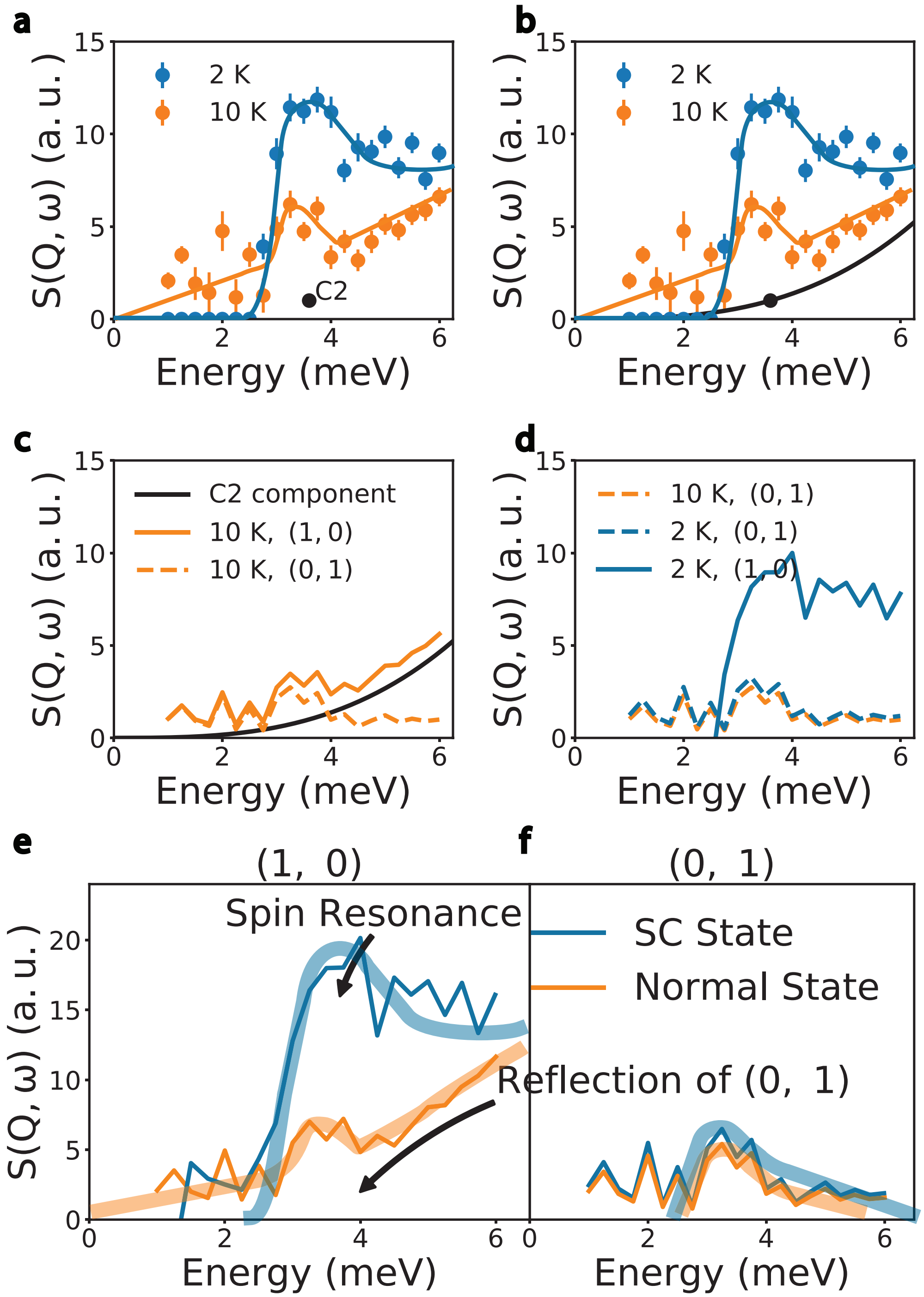

FIG. S10. (a) Energy dependence of the magnetic scattering obtained on the twinned sample from Fig. 1(c). The solid dot indicates the estimated anisotropy C_2 in the normal state from Figs. 4(e) and 4(f) in the detwinned sample. (b) The solid line is the estimated energy dependence C_2 from the detwinned sample by considering data from MAPS, PUMA, and PANDA. Estimated energy dependence of the magnetic scattering at $(1, 0)$ and $(0, 1)$ for the detwinned FeSe using data from (a) for the twinned sample in the (c) normal and (d) superconducting states. Estimated magnetic scattering at (e) $(1, 0)$ (f) $(0, 1)$ across T_c. The solid lines are schematic illustration shown in Figs. 1(f) and 1(g).

S10(c) shows our estimated normal state magnetic scattering for a detwinned sample using twinned sample data of Figure S10(a). Since we do not expect that the detwinning ratio will change across T_c, we can also estimate the situation in the superconducting state. According to our PANDA data in Fig. 4(f), the magnetic resonance at wave vector $(0,1)$ intensity increases about 20% compared with the normal state. We can then simply multiply 120% to the $(0,1)$ intensity in the normal state to get the scattering in superconducting state. By demanding that the intensity sum of $(1,0)$ and $(0,1)$ to be equal to the intensity of twnnined sample divided by 2, we can estimate the intensity of $(1,0)$ and $(0,1)$ in the detwinned case. The solid lines in Figures S10(e) and (f) show our estimated intensity for detwinned sample in the normal and superconducting states. By carrying out this estimation, we note that the actual intensity gain at $(1,0)$ in detwinned case in Figs. 4(e) and 4(f) is somewhat less than that calculated using twinned data. This could be due to statistics of detwinned sample and background. For this reason, the schematic figures in Figs. 1(f) and 1(g) are only an educated estimation of the situation. Note that our basic assumption is a monotonic C_2 component in the normal state and the magnetic intensity goes to zero below $E = 2.5$ meV except at the $(1,0)$ position in the superconducting state.

[1] H. Eschrig and K. Koepernik, *Tight-binding models for the iron-based superconductors*, Phys. Rev. B **80**, 104503 (2009).

[2] P. O. Sprau, A. Kostin, A. Kreisel, A. E. Böhmer, V. Taufour, P. C. Canfield, S. Mukherjee, P. J. Hirschfeld, B. M. Andersen, and J. C. S. Davis, *Discovery of orbital-selective Cooper pairing in FeSe*, Science **357**, 75 (2017).

[3] A. Kreisel, B. M. Andersen, P. O. Sprau, A. Kostin, J. C. S. Davis, and P. J. Hirschfeld, *Orbital selective pairing and gap structures of iron-based superconductors*, Phys. Rev. B **95**, 174504 (2017).

[4] Kreisel, A., Andersen, B. M., & Hirschfeld, P. J. Itinerant approach to magnetic neutron scattering of FeSe: effect of orbital selectivity, Phys. Rev. B **98**, 214518 (2018).

[5] A. Kostin, P. O. Sprau, A. Kreisel, Y. Xue Chong, A. E. Böhmer, P. C. Canfield, P. J. Hirschfeld, B. M. Andersen, and J. C. Séamus Davis, *Visualizing Orbital-selective Quasiparticle Interference in the Hund's Metal State of FeSe*, Nature Materials **17**, 869-874 (2018).

[6] E. Prince, editor, *International Tables for Crystallography, Vol. C*, Wiley (2006).

[7] T. A. Maier, S. Graser, D. J. Scalapino, and P. Hirschfeld, *Neutron scattering resonance and the iron-pnictide superconducting gap*, Phys. Rev. B **79**, 134520 (2009).

[8] M. A. Tanatar, A. E. Böhmer, E. I. Timmons, M. Schütt, G. Drachuck, V. Taufour, K. Kothapalli, A. Kreyssig, S. L. Bud'ko, P. C. Canfield, R. M. Fernandes, and R. Prozorov, *Origin of the Resistivity Anisotropy in the Nematic Phase of FeSe*, Phys. Rev. Lett. **117**, 127001 (2016).

[9] X. Lu, D. D. Scherer, D. W. Tam, W. Zhang, R. Zhang, H. Luo, L. W. Harriger, H. C. Walker, D. T. Adroja, B. M. Andersen, and P. Dai, *Spin Waves in Detwinned* $BaFe_2As_2$, Phys. Rev. Lett. **121**, 067002 (2018).

[10] H. Man, X. Lu, J. S. Chen, R. Zhang, W. Zhang, H. Luo, J. Kulda, A. Ivanov, T. Keller, E. Morosan, Q. Si, and P. Dai, *Electronic nematic correlations in the stress-free tetragonal state of* $BaFe_{2-x}Ni_xAs_2$, Phys. Rev. B **92**, 134521 (2015).

[11] Chong Wang, Rui Zhang, Fa Wang, Huiqian Luo, L. P. Regnault, Pengcheng Dai, and Yuan Li, *Longitudinal spin excitations and magnetic anisotropy in antiferromagnetically ordered* $BaFe_2As_2$, Phys. Rev. X **3**, 041036 (2013).

[12] Q. Wang, Y. Shen, B. Pan, X. Zhang, K. Ikeuchi, K. Iida, A. D. Christianson, H. C. Walker, D. T. Adroja, M. Abdel-Hafiez, X. Chen, D. A. Chareev, A. N. Vasiliev, and J. Zhao, *Magnetic ground state of FeSe*, Nature Communications **7**, 12182 (2016).